

Evolution and Characterization of Pressurized Flow Conditions in Stormwater Collection Networks

Jose G. Vasconcelos¹, Vitor G. Geller², Carolina Triboni³, Daniel B. Wright⁴, and Ben R. Hodges⁵

¹ Department of Civil and Environmental Engineering, Auburn University, 238 Harbert Eng. Center, Auburn, AL 36849, jgv@auburn.edu, corresponding author.

² Department of Civil and Environmental Engineering, Auburn University, 238 Harbert Eng. Center, Auburn, AL 36849, vgg0010@auburn.edu

³ Department of Civil and Environmental Engineering, Auburn University, 238 Harbert Eng. Center, Auburn, AL 36849, czt0059@auburn.edu

⁴ Department of Civil and Environmental Engineering, The University of Wisconsin, Madison, 1415 Engineering Drive, Madison, WI 53706, danielb.wright@wisc.edu

⁵ Maseeh Department of Civil, Architectural, and Environmental Engineering, The University of Texas, Austin, 301 E. Dean Keeton, Austin, TX 78712, hodges@mail.utexas.edu

ABSTRACT

Intense rain events and sprawling urbanization have contributed to more frequent flash flooding in cities, often due to the pressurization of drainage systems. Stormwater collection networks (SCNs) can become pressurized if their conveyance capacity is exceeded, leading to on-street flooding through backflow out of curb inlets. Due to the complexity of SCN geometry and spatiotemporal rainfall variability, studies evaluating pressurization in stormwater systems have previously been conducted for relatively simple geometries and inflow conditions. Thus, to date there have been few network-scale insights into how pressurization develops, making it difficult to understand drivers that influence pressurization: slope, roughness, connectivity, and inflow rate. The present work evaluates the process of SCN pressurization using numerical modeling through a systematic variation of these variables. Herein, three distinct pressurization mechanisms were identified by using EPA SWMM 5.1 to model idealized SCN topology and junction inflows. New non-dimensional flow indexes (NDFI) are proposed to characterize the

pressurization conditions after an initially empty stormwater system reaches steady-state under application of hydrographs. This study provides a basis for further systematic evaluation of factors influencing drainage system pressurization, guiding future actions to mitigate urban flash flooding.

Keywords: Sewer Pressurization, Drainage Systems, SWMM, Numerical Modeling

INTRODUCTION

Stormwater drainage systems are a critical urban infrastructure for public safety, health, and economic development. These systems – hereafter stormwater collection networks (SCN) – include the small-diameter sewer pipes (collecting and conveying water from surface catchments) and the larger conduits, open channels, and detention facilities sized for the accumulated flows from the upstream network. Most SCNs are designed for free-surface flow in closed conduits under expected conditions, but undergo pressurization (i.e., full-pipe flow) during intense rain events when and where the local conveyance capacity is exceeded. Such pressurization or "surcharging" events can cause backflow onto streets, flash flooding, and a host of adverse multiphase flow interactions, such as stormwater geysering and manhole cover displacements. While such events are relatively rare, they are arguably the critical failure mode for SCNs and constitute hazards to life and property. Unfortunately, such hazards will likely become more frequent due to the increasing rainfall intensities attributed to global warming (e.g., Tabari 2020) and continued urbanization (e.g., Chen et al. 2022). Although significant literature exists on the physics and impacts of pressurization at or near the pressurization location, system-wide characterization of the flow conditions and effects of network topology on pressurization behaviors has not been examined. Better understanding of the systemic relationships between rainfall, SCN topology, and pressurization events is needed so engineers can better predict SCN locations likely to see pressurization and potentially hazardous conditions. This study provides numerical experiments to provide the foundations for future studies of SCN pressurization.

As noted above, the local effects of large inflows and subsequent pressurization have been an area of significant experimental contributions for (e.g., Sangster et al. 1958, Wiggert 1972, Trajkovic et al. 1999, Vasconcelos and Wright 2005). The experimental research on local losses in junctions presented by Sangster et al. (1958) considered variables such as conduit arrangement and manhole, inlet grate, outfall entrance, and pipe geometries; however, they analyzed only steady flow, thus providing little insight into how pressurization conditions develop and evolve during filling of an SCN. Other experimental studies have provided valuable insights into the evolution of combined pressurized air and water flows (commonly known as mixed flows) that cause manhole geysers, albeit such studies have been in relatively short systems with simpler single-pipe geometries, in stark contrast with the complex networks that make up real-world SCNs. Numerical investigations have considered mixed-flow conditions in varying local conduit geometries, from simple conduits to complex tunnel systems (e.g., Zhou et al. 2002; Vasconcelos et al. 2009; Leon et al. 2010; Kerger et al. 2012; Cataño-Lopera et al. 2014; Rokhzadi and Fuamba 2020), among others. The few prior studies for system-scale effects begins with the simplified model of Chien and González-Castro (2000), who represented gradually varied flows in complex dendritic (tree-like) SCN geometries using Hydraulic Performance Graphs. Their approach was adopted and expanded by Oberg et al. (2017) to include simulation of flow pressurization, modeling the system-wide evolution of hydraulic grade lines through a sequence of steady-state flow inputs at junctions. The prior studies are limited to dendritic topologies and provide few insights into the time-varying pressurization. Also, existing contributions provide limited information on the pressurization of looped topologies that are common where cross-connections are used to improve distribution of large flows across the SCN.

Large-scale analyses of SCNs are typically conducted with SWMM—the US EPA Storm Water Management Model (Rossman, 2017)—or similar commercial products, which often use modified versions of SWMM as their computational core. The Saint-Venant equations (Hodges, 2019) are the governing equations for open-channel flow in these models. Local areas of pressurized flow are generally handled either through the “Preissmann Slot” (Cunge and Wegner, 1964) or the EXTRAN lumped inertia approach

(Roesner et al. 1988). Both modeling approaches are widely considered adequate for large-scale SCN design and analyses. Indeed, when applied with adequate spatial and temporal discretization, SWMM has been shown to reasonably represent local-scale pressurization phenomena observed in experiments (Ridgeway and Kumpula 2008; Vasconcelos et al. 2018) and transient pressure propagation for both linear topologies (Pachaly et al. 2020) and simple stormwater tunnel systems (Pachaly et al. 2021; Geller and Vasconcelos 2023).

While important progress has been made in understanding the details of *how* pressurization occurs, existing studies cannot provide insights on *where or when* pressurization will likely occur and the systemic causes. The complexity of attaining this answer in real-world SCN stems from the wide range of variability across four categories that define the SCN and its forcing: 1) local conduit geometric characteristics (e.g., slope, diameters, pipe roughness); 2) large-scale system conduit topology (dendritic and looped); 3) spatiotemporal variability of rainfall, and 4) the possible initial (i.e., base flow) conditions throughout the SCN. The underlying variability of the system and its driving inflows makes it challenging to develop a generalized and systemic understanding of behaviors. The present work focuses on how local conduit geometric characteristics influence conduit pressurization onset and evolution for simplified generic large-scale system topologies and rainfall characteristics applied to an initially-dry SCN. The over-arching goal is to understand the flow conditions leading to pressurization-linked failures in stormwater systems so that future studies can devise preventative design methods.

OBJECTIVES

This research has two objectives: (1) classify behaviors of SCNs undergoing pressurization and (2) quantify behaviors using non-dimensional indices that can be applied across a range of SCNs. To accomplish these objectives, EPA SWMM 5.1 is used model to study the onset and evolution of pressurization in SCNs for different topologies, pipe roughness, slope, and inflows. In contrast to prior work using simple single-line conduit, this work evaluates how pressurization behaviors differ in idealized dendritic and looped SCN topologies.

METHODOLOGY

SCN geometries and tested conditions

As a first step towards a general understanding of large-scale SCN behavior, this research conducted 80 numerical simulations (Table 1) that are representative of the variability in SCN topology using SWMM. Simplifications of system variability, as discussed below, were introduced to make this study tractable.

Firstly, this considered only two basic topologies: (1) entirely dendritic and (2) entirely looped, with 11 x 11 junction grids linked by 1-m diameter, 100-m long circular sewers, as illustrated in Figure 1. Most SCN topologies fall somewhere between these two types, typically with dendritic sections that are connected with looped sections that allow shared capacity. By elucidating how pressurization behaviors are affected by these “end-member” topologies, this study provides the foundations for further investigation involving hybrid topologies.

Secondly, the cases studied begin with all conduits dry (zero base flow), so the simulations represent the filling of the SCN under a constant, uniform, rainfall rate that begins with an impulsive start. Finally, it is imposed an impulsively-started, spatially-uniform rainfall that transitions in the first model time step from zero inflow to a uniform steady inflow value at each of the 121 SCN junctions. Junction inflows generated by rainfall are represented by the variable Q_{inflow} , which corresponds to the summation of all junction inflows. The baseline value for Q_{inflow} in this study is $2.10 \text{ m}^3/\text{s}$ (i.e., $0.01735 \text{ m}^3/\text{s}$ per junction), with the values in different simulation cases varying from $1.58 \text{ m}^3/\text{s}$ up to $4.20 \text{ m}^3/\text{s}$. The minimum Q_{inflow} value was selected to ensure the last SCN segment would attain pressurization under any tested slope at least in one reach of the system. For reference, consider fully impervious subcatchments with areas of 100 m x 100 m, and linked to the model junctions. The inflows admitted into each junction would be generated by a steady rain event with intensities varying from 4.70 mm/h to 12.50 mm/h (0.185 in/h to 0.492 in/h).

The studied cases include two values of conduit roughness and five values of conduit slope as outlined in Table 1. Conduit roughness was set uniformly across the domain, with either $n = 0.010$ and $n = 0.016$ as low and moderate values to evaluate the sensitivity of our results to roughness. Additional junction energy losses (i.e., K factors) were not included. Five slopes S_o , ranging from 0.01% to 1.0%, were used. For each slope test condition, a single slope was applied uniformly over the domain so that each junction has identical upstream and downstream slopes connecting with a junction. The outfall junction is a free discharge to atmospheric pressure through an upstream outflow conduit at a horizontal slope. Thus, this study introduces variability through the conduit slope and roughness, affecting its conveyance capacity, and the rainfall intensity, which sets the overall forcing level.

The test cases are all transitions from an empty SCN to steady flow throughout, which occurs when the sum of the Q_{inflow} is nearly equal to the outflow. The criteria used to determine when an SCN reaches steady conditions is when the outflow rate reached 99% of Q_{inflow} ; the corresponding time is denoted as T_{Q99} . The time interval $[0, T_{Q99}]$ is the range over which the sudden introduction of the inflows can lead to sewer pressurization. It was observed that the final 1% of flow adjustments to the steady state are small and do not impact pressurization dynamics. However, the additional time required to achieve 100% is long and is likely related to numerical convergence of the SWMM hydraulic solver rather than flow physics. Thus, the data for the analysis herein are aggregated over the $[0, T_{Q99}]$ interval.

In summary, this work introduces system and inflow simplifications to enable assessment of how pressurization evolves within SCNs in response to intense rain events. While the sewer geometry, topologies, and inflow conditions are not representative of any specific drainage network, this conceptual investigation provides new data on pressurization behavior that may provide insights into pressurization evolution of more complex drainage systems.

SWMM implementation

The implementation of the SWMM models representing the SCN and the process of pressurization is described here. Typical SWMM models have subcatchments linked to rain gauges that generate runoff, which is eventually admitted into junctions and conduits. By contrast, the fixed inflows were admitted into junctions through time series, and thus there was no need for rain gauges or subcatchments in the tested models. Each manhole in the model was represented through a SWMM junction, and there was no sub-discretization of conduits, thus characterizing the typical link-node approach used in most SWMM models.

The mathematical model used in the SWMM simulations was the Dynamic Wave, thus the Saint-Venant equation, in which the inertial terms were kept. The criteria for determining maximum flow to normal flow (i.e., normal flow criterion) was based on Slope and Froude number, based on the recommended approach in current SWMM versions. Rather than enable variable time step, simulations were performed with a fixed routing time step of 1 second, and the head convergence tolerance was set to 0.0015 m. Finally, some initial simulations applied EXTRAN as the pressurization algorithm, but numerical instabilities were noticed in some of the tested conditions. Thus, all simulations presented here were performed using the built-in Preissmann Slot pressurization algorithm (i.e., SLOT).

Non-dimensional Flow Indexes

This work introduces eight normalized, non-dimensional flow indexes (NDFI), as presented below, for data analyses. The local non-dimensional flow depth for the j junction is defined as D_j^* , and provides the base for computing an average non-dimensional flow depth, D_{avg}^* , for all junctions for a given combination of Q_{inflow} , topology, slope, and roughness:

$$D_j^* = D_j/d \quad (1)$$

$$D_{avg}^* = \frac{1}{N_j} \sum_{j=1}^{N_j} D_j^* \quad (2)$$

The local non-dimensional flow rate of the i^{th} pipe flow, Q_i^* is normalized using the idealized Chezy-Manning flow for a full pipe (Q_f) as the flow scale. Thus, $Q_i^* > 1$ is indicative of flow rates exceeding the theoretical free-flow conveyance and is an indicator of pressurized flow. The Q_i^* are used to construct two additional NDFIs: Q_{avg}^* and Q_{max}^* . These are respectively the average and maximum Q_i^* values across all conduits for a given simulation condition. As the base Q_i^* are normalized by the theoretical full pipe flow, values of Q_{avg}^* and Q_{max}^* metrics near or greater than unity denote flow conditions in which more of the conduit flows are close to or exceed the theoretical full flow capacity. It follows that higher values are linked to a greater number of junctions in pressurized flow conditions.

$$Q_i^* = \frac{Q_i}{\left(\frac{1}{n}\right) \frac{\pi}{2^{10/3}} d^{8/3} \sqrt{S_o}} = \frac{Q_i}{Q_f} \quad (3)$$

$$Q_{max}^* = Q_{inflow}/Q_f \quad (4)$$

$$Q_{avg}^* = \frac{1}{N_c} \sum_{i=1}^{N_c} Q_i^* \quad (5)$$

Two NDFI are proposed relating energy losses due to friction and available potential energy expressed in terms of pipe slope:

$$R_{f,i}^* = S_{f,i}/S_o \quad (6)$$

$$R_{f,avg}^* = \frac{1}{N_c} \sum_{i=1}^{N_c} R_{f,i}^* \quad (7)$$

$R_{f,i}^*$ is the ratio between the slope of the hydraulic grade line and the conduit slope S_o . Values of hydraulic grade line $S_{f,i}$ are evaluated with SWMM results for the head difference in consecutive junctions over a conduit length as $S_{f,i} = \Delta H/L_i$. The corresponding system-wide average of $R_{f,i}^*$ for a given condition is $R_{f,avg}^*$. Near-unity $R_{f,i}^*$ values were observed in conduits where flows are near uniform conditions and low $R_{f,i}^*$ were observed in conduits experiencing backwater effects in the SCN, i.e., large depths with relatively low flows.

Each NDFI is time-varying as the system fills, but for pressurization analysis we are interested in the NDFI values at T_{Q99} when further changes in the pressurization are minor. To evaluate time-varying behavior across different simulations, a non-dimensional time T_{Q99} is introduced using the ratio between Q_{inflow} and the total storage provided by the conduits, the latter defined as $V_{SCN} = \frac{\pi}{4} d^2 \sum_{i=1}^{N_c} L_i$:

$$T_{Q99}^* = \frac{T_{Q99}}{Q_{inflow}/V_{SCN}} \quad (8)$$

RESULTS AND DISCUSSION

Comparison between SWMM and manual computation of SCN pressurization

For verification purposes, the simulation results of the hydraulic grade line (HGL) when the system reached near-steady state were compared in selected cases to results from manual calculation applying the energy equation. The selected cases involved two n values of 0.010 and 0.016, and slopes of 0.0001. For all cases, the two-way connectivity was used to facilitate manual calculations of HGL junction to junction, and the results are presented in the profile from junction A00 to the outfall shown in Figure 2. As with the calculations in SWMM, no local losses were considered in the manual calculations. For this comparison, the two pressurization algorithms in SWMM (SLOT and EXTRAN) were used.

It can be noted that the SWMM-derived HGL follows the results obtained with the application of the energy equation, with the former presenting consistently slightly smaller pressures for the smaller roughness case. The explanation for the difference lies in the SLOT algorithm implementation within SWMM 5.1.15, which considers the area within the slot in the computation of the reach velocity, and with that the friction losses. The manual computation simply considered the pipe cross-sectional area, yielding then slightly larger velocities which explains the differences in the energy losses. Performing the manual HGL calculation considering slot area in the flow yielded near identical results to SWMM HGL calculations. Nevertheless, these results indicated that the SWMM pressurization profiles are representative of the ones anticipated in the SCNs considered in this work.

Classification of SCN pressurization processes

Based on the direct observation of the evolution of the HGL and subsequent conduit pressurization, a classification scheme is proposed to characterize the pressurization process, as follows:

- Type A pressurization: downstream initiation, no upstream progression. The system pressurization is observed only in the final junctions, i.e., K10, K09, J09, and J10, due to the bottleneck created by the single outflow pipe that must handle the entire flow. All other junctions in the system remained in the free-surface flow regime at steady-state conditions, as shown in Figure 3. This behavior was typical for steeper slopes ($S_o = 0.5\%-1\%$), lower values of Manning roughness, and SCN topologies with four-way connectivity.
- Type B pressurization: downstream initiation, upstream progression. For these cases, the pressurization is first observed near the outfall, similar to Type A, due to a bottleneck effect from the outlet. However, because the average conduit conveyance was smaller in these cases, the pressurization interface had a slow upstream progression, as shown in Figure 4. This behavior was typical of intermediate slopes ($S_o \approx 0.05\%-0.5\%$) and for SCNs with four-way connectivity. These conditions result in the largest T_{Q99} values, requiring longer times to reach steady state.
- Type C pressurization: midstream initiation, upstream and downstream propagation. For these cases, conveyance in the conduits is very limited and more significant than the bottleneck effect at the SCN outlet conduit. As a result, the pressurization initiates some distance upstream from the outlet, indicating the downstream outlet is *not* the flow constriction causing pressurization. The initial location of Type C pressurization depends on the interaction of flow conditions and system topology. The pressurization region propagates upstream and downstream from the initial point, as shown in Figure 5. These conditions were observed most frequently for slopes under 0.1%, higher Manning roughness values, and most commonly for SCNs with two-way connectivity. The steady-state condition typically shows pressurization throughout the system for Type C pressurization.

Type C pressurization is characterized by fast propagation of pressurization fronts, which is likely to play a role in the development of manhole geysers.

The Type B and C behaviors from Figures 3 and 4 can be illustrated with network maps of pressure head and flow depths at T_{Q99} , as shown in Figure 6. These results indicate a complex condition in which conduits are all in gradually varied flow mode upon reaching steady state. However, in some of the tested cases, steady hydraulic jumps were noticed in the HGL profiles via abrupt changes in flow depth. The results presented in Figures 3 to 6 are relevant in that they indicate how the pressurization developed over time, where pressurization was initiated, and how it developed over time for each tested case. As shown later, the development of Type C pressurization typically occurred more rapidly than Type B, explaining why some portions of SCN pressurize faster than others. Conversely, if the pressurization of an SCN can be classified as Type B, changes in junction heads may occur very slowly. These findings were also valid for the cases that were run with the other Q_{inflow} values: 1.58 m³/s, 3.15 m³/s, and 4.20 m³/s. The simulated pressurization evolution could also be classified into these three pressurization types for all other cases.

Table 2 presents all the results for Q_{max}^* and the observed pressurization types for all tested cases, grouped by SCN topology (two-way or two-way). SCN connectivity had a strong effect on energy losses and hence, on junction pressurization. The table also presents values for Q_{max}^* calculated from equation 4, which were correlated with the observed pressurization type. It was noticed that, for certain cases, the pressurization types varied from A to B or from B to C as Q_{max}^* increased due to larger junction inflows.

The results presented in Table 2 also indicate a relationship between connectivity, the values for Q_{max}^* , and the corresponding pressurization type. The smallest values of Q_{max}^* were linked to pressurization types A and B, with the largest Q_{max}^* values linked with pressurization type C. For two-way connectivity SCNs, all conditions with Q_{max}^* above 3.1 yielded a type C pressurization. None of the simulations considering four-way connectivity resulted in type C pressurizations and all tested conditions with $Q_{max}^* > 2.3$ yielded type B pressurization type. These relationships can also be observed in the diagram presented in Figure 7. Results for $Q_{max}^* > 7$ were omitted since pressurization types did not change for larger Q_{max}^* .

Summarizing the effects of the selected variables in the pressurization characteristics

The results presented in Table 2 and Figure 7 enable us to have a general understanding of some factors that are important regarding the evolution of pressurization in SCN, as summarized below:

- The better junction connectivity in four-way topologies (looped) had a major impact in reducing the overall pressure build-up in SCNs, particularly in intermediate reaches of SCN topologies. As a result, only Type A or B pressurization mechanisms were observed for four-way topologies.
- Slope was also a major factor influencing the pressurization type for two-way (dendritic) topologies. Most conditions (23 out of 24) with slopes equal or smaller than 0.1% result in Type C pressurization. Conversely, no Type C pressurization occurred for slopes of 0.5% and two-way topologies, and in such cases the pressurization type depended on the roughness, and Q_{inflow} .
- While all types of pressurization types were observed in conditions with lower Manning roughness, far fewer cases of Type A pressurization (5 out of 40) were observed for conditions with the higher Manning value. This suggests that rougher conduits will lead to more widespread pressurization across SCNs.

Characterization of flows in pressurized SCN using the proposed NDFI

The second objective of this work is to characterize flow conditions in SCN systems that experience pressurization conditions. This characterization is done by comparing pressure heads, energy losses, and the time for the SCNs to reach steady flow conditions for each tested case. Although these results depend on the selected SCNs' topology, it is hypothesized that the relationships between the NDFI is similar for system topologies that have a mix of dendritic and looped sections.

The initial calculations were performed for the baseline flow $Q_{inflow} = 2.1 \text{ m}^3/\text{s}$ when all 121 junctions received a fixed inflow of $0.01735 \text{ m}^3/\text{s}$. For these inflow conditions, twenty unique cases were evaluated, considering the five tested slopes, two Manning roughness values, and two connectivity

topologies. The results for the system-wide average junction flow depths D_{avg}^* were computed for each case and the results are presented in Figure 8 along with pressurization types in terms of Q_{avg}^* . Results in Figure 8 are grouped by connectivity and slope as the results for the shallower slopes (0.01%, 0.05%, and 0.10%) are separated from the results with steeper slopes (0.50% and 1.0%).

Figure 8 shows that, as expected, D_{avg}^* increases with Q_{avg}^* . Higher flow rates lead to higher energy losses and pressure build-up, which is reflected in the average junction depth. Figure 8 also shows that Q_{avg}^* and D_{avg}^* are consistently higher in dendritic SCNs than in looped SCNs for the same conditions of slope and roughness; this is an expected result since the total flow is more widely distributed across conduits given the greater connectivity in the looped SCNs. The smallest Q_{avg}^* values were also linked with the smallest D_{avg}^* values observed for the SCNs with steeper conduit slopes, both in the looped and dendritic SCNs. Steeper slopes were linked to higher conduit conveyance (i.e., Q_f) and smaller Q_{avg}^* values, decreasing junction pressure build-up in the SCN and leading to smaller D_{avg}^* values.

Since friction losses and hence $R_{f,avg}^*$ increase with flow rates, it was expected to observe a positive correlation between Q_{avg}^* and $R_{f,avg}^*$, as shown in Figure 9 for shallower slopes. However, this was not observed in the conditions with steeper reach slopes ($S_o \leq 0.5\%$). For conditions with steeper slopes, the calculated energy slopes across the SCN were closer, albeit slightly under, the reach slope S_o , signaling reduced backwater effects and $R_{f,avg}^*$ values closer to unity. For shallower slopes, the SCN connectivity influenced the final configuration of the hydraulic grade lines. The gradual flow increases for dendritic SCN with shallower slopes resulted in increasingly higher velocities and steeper HGL as flows moved downstream, creating an HGL profile with downward concavity. As the flows were combined in the collection branch between junctions A10 and K10, the energy slope became even steeper. However, for most looped SCN, the flow distribution through more reaches mitigated the increasing HGL slope between reaches, and the resulting system-wide HGL resembled a 2-D plane and comparatively smaller $R_{f,avg}^*$

values, as illustrated in Figure 10. This result agrees with the results shown in Figure 8 and suggests that looped SCN in the real world will be less prone to pressurization and flash flooding.

The time required for the SCNs to achieve a steady state, T_{Q99}^* , has a strong dependence on slope and connectivity, as shown in Figure 11. For most cases with steeper slopes, the values of T_{Q99}^* were small and increased with the Q_{avg}^* , typically attaining a steady state in less than two hours, or $T_{Q99}^* < 0.1$. The values for T_{Q99}^* were consistently much higher for conditions with shallower slopes, but an interesting decrease in T_{Q99}^* was observed as Q_{avg}^* values increased. Because all such cases involved pressurization Types B or C, steady-state conditions were only achieved after the pressurization process within the SCN was completed. Larger Q_{avg}^* values were linked to decreased Q_f and decreased conveyance capacity, leading to quicker pressurization of junctions and conduits and, consequently, shorter T_{Q99}^* . While there was a significant difference in T_{Q99}^* values for the tested SCN connectivity, the normalized T_{Q99}^* is comparable between the looped and dendritic SCNs.

Effect of varying inflow contributions at junctions in SCN pressurization

This section explores modeling results with additional simulations in which Q_{inflow} was varied from the baseline of $2.1 \text{ m}^3/\text{s}$. A direct correlation between Q_{inflow} and Q_{avg}^* exists and, as inflows increased, there is an increase in the average flow depth at junctions D_{avg}^* , as shown in Figure 12. For values of $Q_{avg}^* > 0.25$, the data appears to follow two trends; unfortunately, these trends are not related to a single variable, such as slope, connectivity, or roughness, but rather to combinations of these variables.

In terms of $R_{f,avg}^*$, the observations made for the $Q_{inflow} = 2.1 \text{ m}^3/\text{s}$ are also applicable for all other inflows, as shown in Figure 13. Most studied cases having $Q_{avg}^* < 0.15$, typically associated with steeper conduit slopes, had corresponding $R_{f,avg}^*$ values above 0.6, indicating that the friction slope values were near S_o values, indicating little to no significant backwater effects impacting the friction slope. For shallower slopes, a direct relationship between Q_{avg}^* and $R_{f,avg}^*$ was observed.

Finally, as is shown in Figure 14, the variation of Q_{inflow} influences the peak of T_{Q99}^* values, as larger junction inflows increase the steady-state flows across the SCNs. On the other hand, the general relationship between T_{Q99}^* and Q_{avg}^* is not significantly influenced by variations of Q_{inflow} . The smallest values of Q_{avg}^* is linked with the smallest T_{Q99}^* , with a peak appearing for values of Q_{avg}^* around 0.20, followed by a decrease and stabilization of T_{Q99}^* after $Q_{avg}^* > 0.4$.

Broader implications

This study has considered only a limited set of variability in system with idealized topologies and inflow conditions, and its driving boundary conditions. Nevertheless, the results show a rich set of complex interactions that lead to three types of pressurization behavior that depend on both the local conduit geometry and the large-scale network topology. It seems likely that real world systems – with combinations of dendritic and looped sections and spatiotemporally varying rainfall – will see behaviors that have local similarities to types A, B and C pressurization. However, it also seems unlikely that any sufficiently large system will be simply characterized as type A, B, or C pressurization. For practical applications, it is believed that these concepts will be useful in classifying how behavior changes across a system and through time under a variety of forcing; e.g., it may be useful to analyze flow conditions that lead to a network section with type C pressurization (midstream pressurization and propagating both directions) being located upstream of a network section with type B pressurization (beginning downstream and propagating upstream), which could indicate a propensity for trapping air and developing the preconditions for a manhole geyser. Further development of the NDFI metrics and the pressurization types should be focused on linking complex model results to these behaviors so that a large number of simulations can be run on a real-world network to classify and identify likely conditions and locations of pressurization problems.

CONCLUSIONS

Urbanization and more intense rain events have been pushing urban drainage systems into abnormal operation conditions, including more frequent conduit pressurization, surficial flooding, geysering, etc. Numerical modeling tools to represent such flows have improved, and our understanding of air-water interactions in sewers has expanded. Nonetheless, understanding the onset, evolution, and characterization of pressurized flows in SCNs remains limited due to the complexity of conduit geometries, junction connectivity, and spatiotemporal variability of extreme rainfall.

Through a systematic numerical investigation, this work has characterized how the pressurization process evolves in SCNs with different topologies, slopes, and roughness. A key simplifying assumption was that steady inflows were admitted uniformly at all junctions in the system. Various NDFI were constructed with conduit slopes, diameters, and roughness, to represent normalized flow parameters representing system flows, junction depths, energy dissipation, and time for steady flows to be established. These NDFI were calculated for all 80 configurations using SWMM 5.1 model as the conditions in the SCNs became steady.

Three different pressurization types were identified in the tested SCNs. For conditions associated with larger conduit conveyance – steeper slopes, lower roughness, and looped connectivity – pressurization types A and B were observed, starting at the system's downstream end due to the bottleneck. A difference between these two pressurization types is the gradual advance of pressurization fronts in type B due to more limited conveyance. By contrast, Type C pressurization conditions were characterized by junctions in the middle of the SCN as the ones first becoming pressurized and propagating pressurization conditions toward the downstream end. Type C pressurization can potentially facilitate air pocket entrapment if other pressurization fronts form at the downstream reaches of SCN and move toward pressurized upstream junctions.

Values of T_{Q99} , representing the time required to establish steady flow conditions, varied widely in the tests, with the longest time associated with Type B pressurization and looped SCNs. This indicates that systems with larger conveyances will take longer to attain steady pressurization, possibly indicating that such systems are less prone to flash flooding. When considering the normalized T_{Q99}^* , however, the normalized steady-state time was more comparable between dendritic and looped SCN. For the two SCN topologies used in this work, T_{Q99}^* was shown to have a maximum at Q_{avg}^* around 0.20, with a peak T_{Q99}^* values increasing with Q_{inflow} . This finding can be useful for understanding the time required for a given SCN to experience pressurization or surface flooding, which can be useful when devising strategies to mitigate related operational issues.

By using a SCN with 11 x 11 regular junction arrangement, it was possible to better compare the effects of improved flow distribution afforded by looped topologies when contrasted with dendritic ones. Follow up studies should consider other SCN configurations—including real systems—as there are numerous alternatives for looped or combinations of looped and branched SCN topologies. Future research should also consider SCN subjected to highly non-uniform inflows and how pressurization evolves in such conditions. Finally, alternative approaches to characterize pressurization within SCNs in more quantitative fashion can be potentially developed in future studies.

It is hoped that the proposed NDFI could also provide insights for other SCN geometries regarding the pressurization threshold and the severity and spread of junction pressurization, among other factors. Additional studies should include how realistic spatiotemporal rainfall variability could affect the development and spread of pressurized conditions in SCNs. Another potential area for study is tracking displaced air in SCNs during the pressurization process, which could be beneficial for air management in urban drainage systems.

DATA AVAILABILITY STATEMENT

All data and models that support the findings of this study are available from the corresponding author upon reasonable request.

ACKNOWLEDGEMENTS

The authors would like to acknowledge the support by the National Science Foundation under Grants No. 2049025, 2049094, and 2048607.

REFERENCES

- Cataño-Lopera, Y. A., T. E. Tokyay, J. E. Martin, A. R. Schmidt, R. Lanyon, K. Fitzpatrick, C. F. Scalise, and M. H. García. 2014. "Modeling of a Transient Event in the Tunnel and Reservoir Plan System in Chicago, Illinois." *J. Hydraulic Eng.*, 140 (9): 1–12. [https://doi.org/10.1061/\(ASCE\)HY.1943-7900.0000888](https://doi.org/10.1061/(ASCE)HY.1943-7900.0000888)
- Chen, S., Huang, Q., Muttarak, R. Fang, J., Liu, T., He, C., Liu, Z., Zhu, L. (2022) Updating global urbanization projections under the Shared Socioeconomic Pathways. *Sci Data* 9, 137. <https://doi.org/10.1038/s41597-022-01209-5>
- Cunge, J. A., and M. Wegner. 1964. "Intégration numérique des équations d'écoulement de barré de Saint-Venant par un schéma implicite de différences finies." *La Houille Blanche*, 50 (1): 33–39. <https://doi.org/10.1051/lhb/1964002>
- Geller, V.G. and Vasconcelos, J.G. (2023). "Effect of Modeling Setup Parameters in SWMM Predictions of Large-Scale Tunnel Filling" *Proceedings World Environmental and Water Resources Congress 2023: Adaptive Planning and Design in an Age of Risk and Uncertainty* Edited by Sajjad Ahmad, Ph.D., P.E.; and Regan Murray, Ph.D.

417 Hodges, B.R. (2019) "Conservative finite-volume forms of the Saint-Venant equations for hydrology and
 418 urban drainage." *Hydrology and Earth System Sciences*, 23:1281-1304. [https://doi.org/10.5194/hess-23-](https://doi.org/10.5194/hess-23-1281-2019)
 419 [1281-2019](https://doi.org/10.5194/hess-23-1281-2019)

420 Kerger, F., P. Archambeau, B. J. Dewals, S. Erpicum, and M. Pirotton. (2012). "Three-phase bi-layer model
 421 for simulating mixed flows." *J. Hydraulic Res.*, 50 (3): 312–319.
 422 <https://doi.org/10.1080/00221686.2012.684454>

423 Leon, A. S., M. S. Ghidaoui, A. R. Schmidt, and M. H. Garcia. (2010). "A robust two-equation model for
 424 transient-mixed flows." *J. Hydraulic Res.*, 48 (1): 44–56. <https://doi.org/10.1080/00221680903565911>

425 Oberg, O., Schmidt, A.R., Landry, B. J., Leon, A.S., Waratuke, A.R., Mier, J. M., García, M.H. (2017)
 426 "Improved understanding of combined sewer systems using the Illinois Conveyance Analysis Program
 427 (ICAP)", *Urban Water Journal*, 14:8, 811-819, <https://doi.org/10.1080/1573062X.2016.1269811>

428 Pachaly, R. L., J. G. Vasconcelos, D. G. Allasia, R. Tassi, and J. P. P. Bocchi. 2020. "Comparing SWMM
 429 5.1 Calculation Alternatives to Represent Unsteady Stormwater Sewer Flows." *J. Hydraulic Eng.*, 146
 430 (7): 1–16. [https://doi.org/10.1061/\(asce\)hy.1943-7900.0001762](https://doi.org/10.1061/(asce)hy.1943-7900.0001762)

431 Pachaly, R. L., J. G. Vasconcelos, and D. G. Allasia. 2021. "Surge predictions in a large stormwater tunnel
 432 system using SWMM." *Urban Water Journal*, 18 (8): 577–584.
 433 <https://doi.org/10.1080/1573062X.2021.1916828>

434 Rigdway, K., and G. Kumpula. 2008. "Surge Modeling in Sewers using Alternative Hydraulic Software
 435 Programs." *J. Water Management Modeling*, 6062: 155–164. <https://doi.org/10.14796/jwmm.r228-10>.

436 Roesner, L. A., Aldrich, J. A., Dickinson, R. E., & Barnwell, T. O. (1988). Storm water management model
 437 user's manual, Version 4: EXTRAN Addendum. Environmental Research Laboratory, Office of
 438 Research and Development, US Environmental Protection Agency.

439 Rokhzadi, A., and M. Fuamba. 2020. "Shock-Fitting Approach for Calculating Air Pocket Entrapment
 440 Caused by Full Obstruction in Closed Conduit Transient Flow." J. Hydraulic Eng., 146 (11): 1–13.
 441 [https://doi.org/10.1061/\(asce\)hy.1943-7900.0001817](https://doi.org/10.1061/(asce)hy.1943-7900.0001817)

442 Rossman, L. A. (2017). Storm Water Management Model Reference Manual Volume II – Hydraulics. U.S.
 443 Environmental Protection Agency, 1–190.

444 Sangster, W. M., H. W. Wood, E. T. Smerdon, and H. G. Bossy. (1958). Pressure changes at storm drain
 445 junctions. Eng. Exp. Station. Univ. Missouri.

446 Tabari, H. (2020) "Climate change impact on flood and extreme precipitation increases with water
 447 availability". Sci Rep 10, 13768 (2020). <https://doi.org/10.1038/s41598-020-70816-2>

448 Trajkovic, B., M. Ivetic, F. Calomino and A. D'Ippolito. (1999). "Investigation of Transition from Free
 449 Surface to Pressurized Flow in a Circular Pipe." Water Science and Technology 39 (9): 105–12.
 450 <https://doi.org/10.2166/wst.1999.0453>

451 Vasconcelos, J. G., and Wright, S. J. (2005). "Experimental Investigation of Surges in a Stormwater Storage
 452 Tunnel." J. Hydraulic Eng., 131: 8. [https://doi.org/10.1061/\(ASCE\)0733-9429\(2005\)131:10\(853\)](https://doi.org/10.1061/(ASCE)0733-9429(2005)131:10(853)).

453 Vasconcelos, J. G., Wright, S.J., and Roe. P.L. (2009). "Numerical oscillations in pipe-filling bore
 454 predictions by shock-capturing models." J. Hydraulic Eng., 135: 4.
 455 [https://doi.org/10.1061/\(ASCE\)0733-9429\(2009\)135:4\(296](https://doi.org/10.1061/(ASCE)0733-9429(2009)135:4(296)

456 Vasconcelos, J. G., Y. Eldayih, Y. Zhao, and J. A. Jamily. 2018. "Evaluating storm water management
 457 model accuracy in conditions of mixed flows." J. Water Management Modeling, 1–10.
 458 <https://doi.org/10.14796/JWMM.C451>

459 Wiggert, D. 1972. "Transient Flow in Free-Surface, Pressurized Systems." J. Hydraulic Div., 98 (1): 10–
 460 27. <https://doi.org/10.1061/JYCEAJ.0003189>

461 Yen, B.C. and Gonzales-Castro, J.A. (2000), "Open-Channel Capacity Determination Using Hydraulic
462 Performance Graph", J. Hydraulic Eng., 126 (2): 112–122. [https://doi.org/10.1061/\(ASCE\)0733-](https://doi.org/10.1061/(ASCE)0733-9429(2000)126:2(112))
463 [9429\(2000\)126:2\(112\)](https://doi.org/10.1061/(ASCE)0733-9429(2000)126:2(112))

464 Zhou, F., F. E. Hicks, and P. M. Steffler. 2002. "Transient Flow in a Rapidly Filling Horizontal Pipe
465 Containing Trapped Air." J. Hydraulic Eng., 128 (June): 625–634. [https://doi.org/10.1061/\(ASCE\)0733-](https://doi.org/10.1061/(ASCE)0733-9429(2002)128:6(625))
466 [9429\(2002\)128:6\(625\)](https://doi.org/10.1061/(ASCE)0733-9429(2002)128:6(625)).

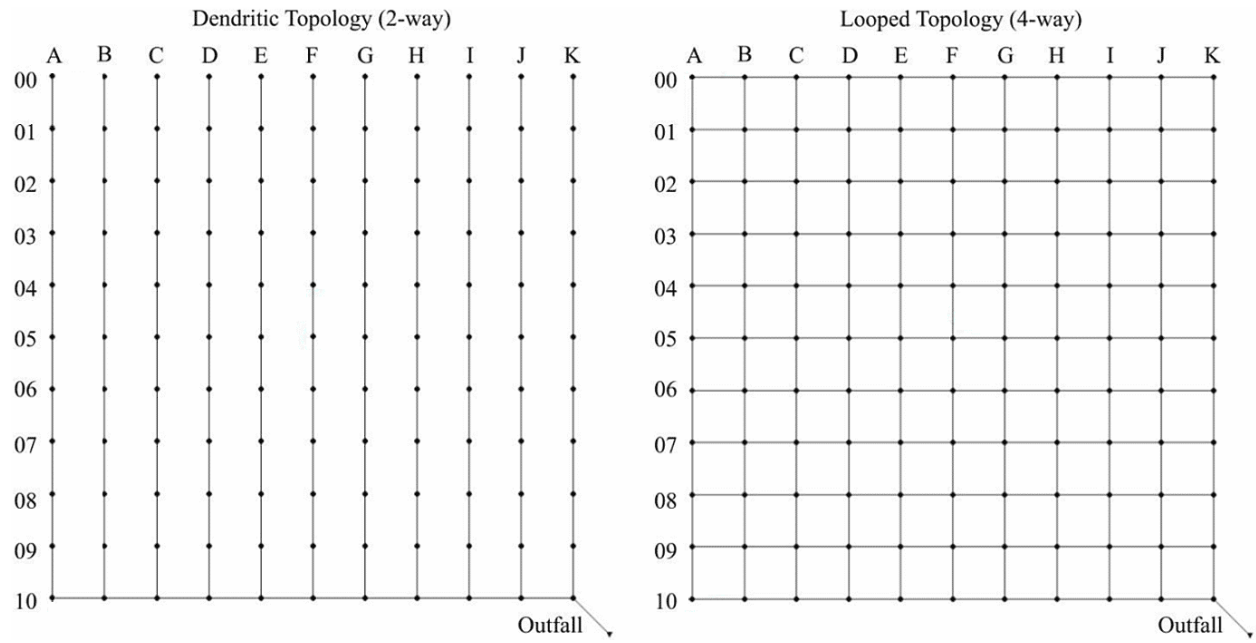


Figure 1: The two idealized SCN topologies, dendritic (two-way) and looped (four-way), that are used in this study. Rainfall inflows are forced on each junction (black dot). Flows in the dendritic topology are always from top to bottom, except for the bottom collection conduit, where flows are from left to right. In the looped topology, the flow directions depend on the local hydraulic grade line.

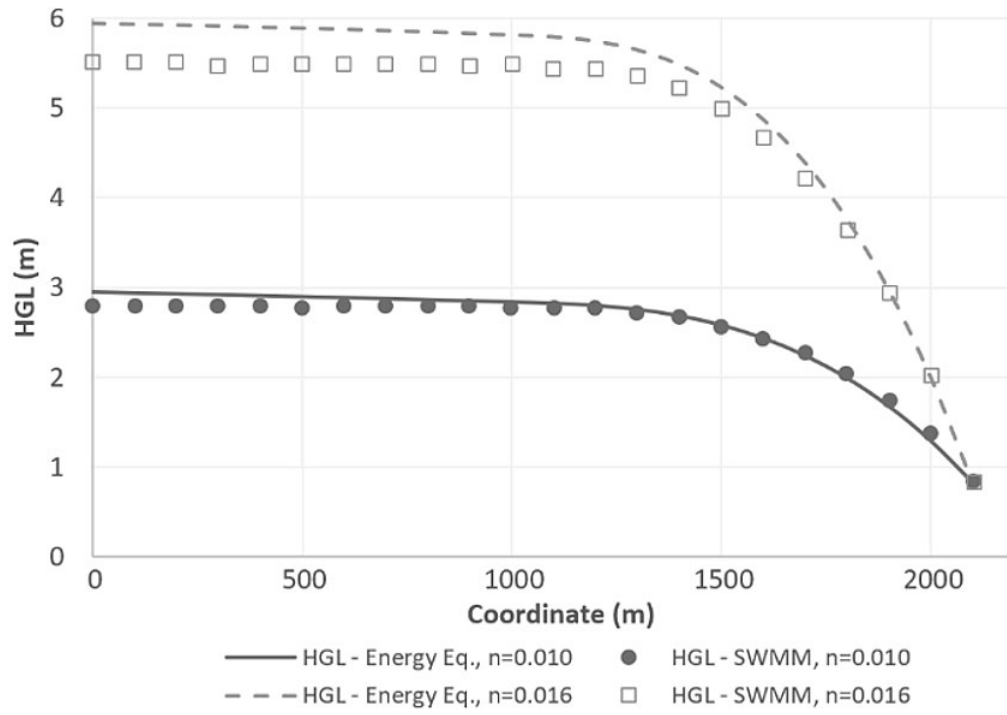
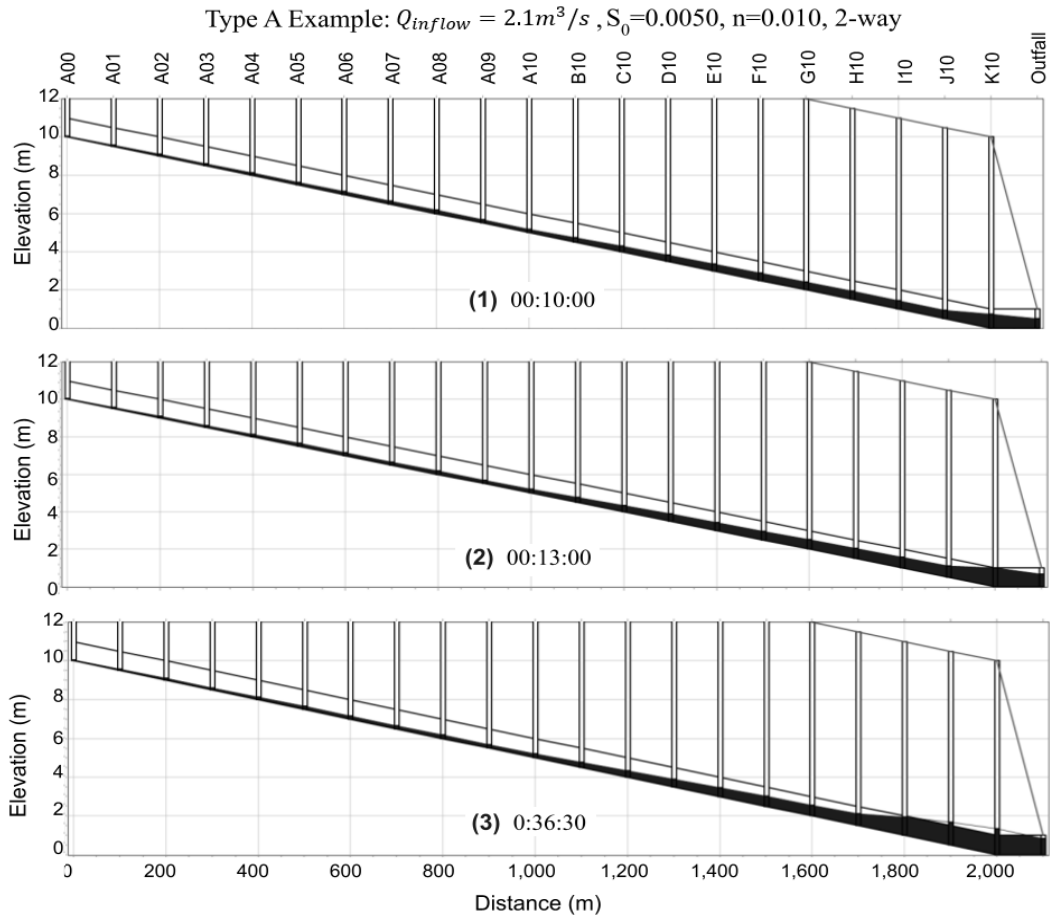


Figure 2: Comparison of HGLs computed by SWMM and calculated with using steady state energy equation between junctions, considering two-way connectivity topology and two Manning roughness values.

10



11

12

Figure 3: Type A pressurization. Frames show HGL between the furthest-upstream junction A00 and outlet.

13

Pressurization occurs only in the 200 m of the conduits connecting nodes I10/J10 and J10/K10 along this profile.

14

The pressurization stabilizes at T_{Q99} , which occurs at the time 0h:37m:30s and does not show further upstream

15

progression.

16

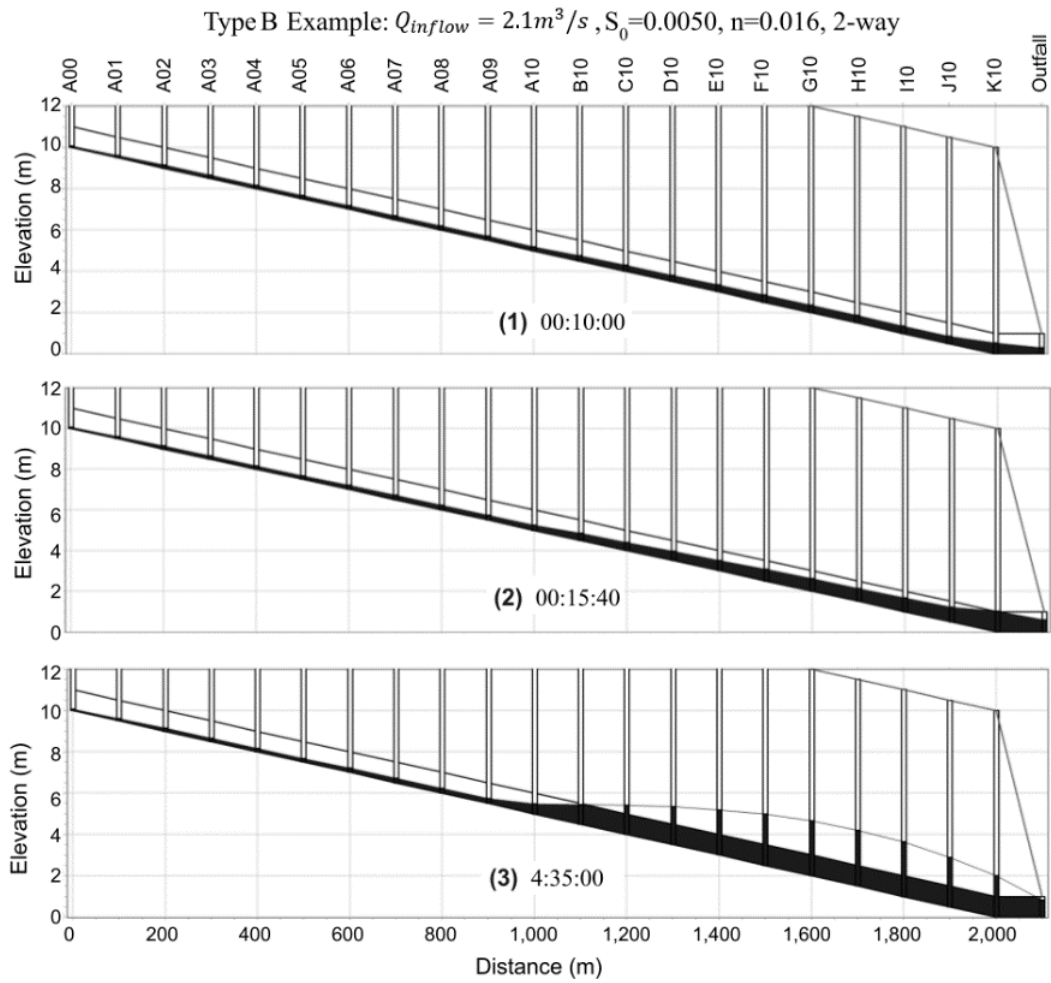


Figure 4: Type B pressurization. Frames show HGL between the furthest-upstream junction A00 and outlet. Pressurization begins at the conduit upstream of K10 and progressively moves upstream to stabilize at B10 at T_{Q99} , which occurs at 4h:35m.

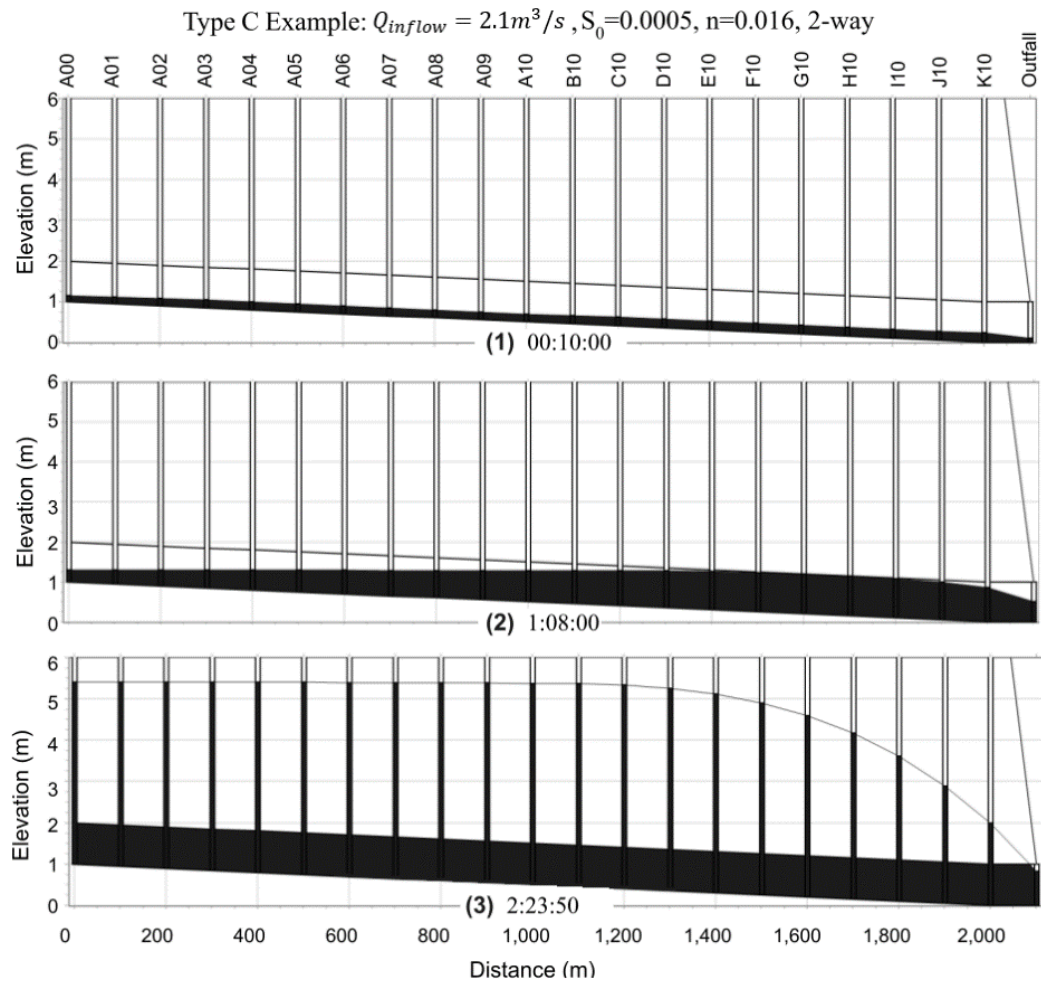


Figure 5: Type C pressurization: midstream initiation, upstream and downstream propagation. Frames show HGL between the furthest-upstream junction A00 and outlet. The pressurization onset occurs at upstream junction G10 at time 1h:08m, with T_{Q99} occurring at 2h:24m.

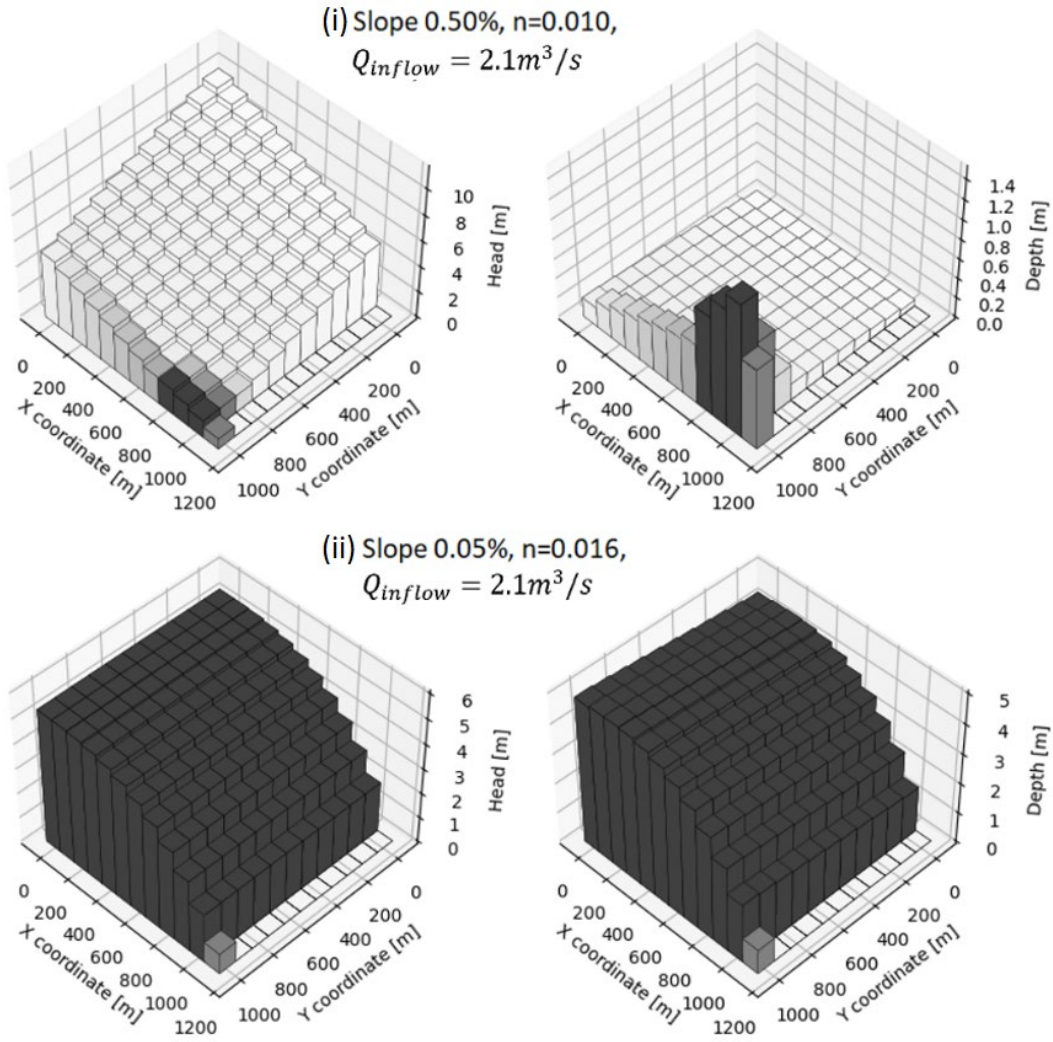


Figure 6: Network-wide distribution of head and depth for dendritic SCN at steady-state (T_{Q99}) flow conditions for (i) Type B pressurization and (ii) Type C pressurization. Dark grey colors represent junctions that are pressurized.

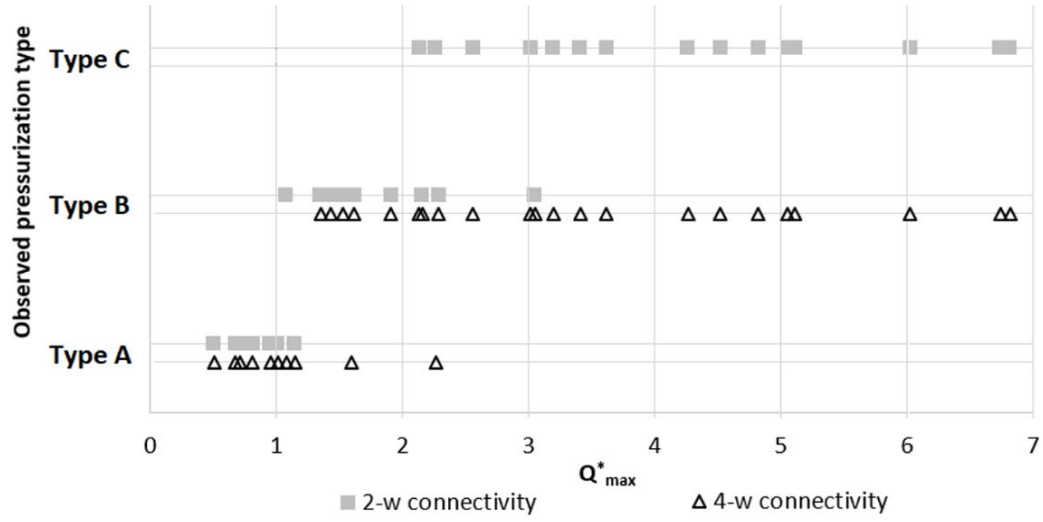


Figure 7: Relationships between the observed pressurization type, SCN connectivity and $Q^*_{max} \leq 7.0$. All other tested cases with four-way and two-way connectivities had Type C and B pressurization, respectively.

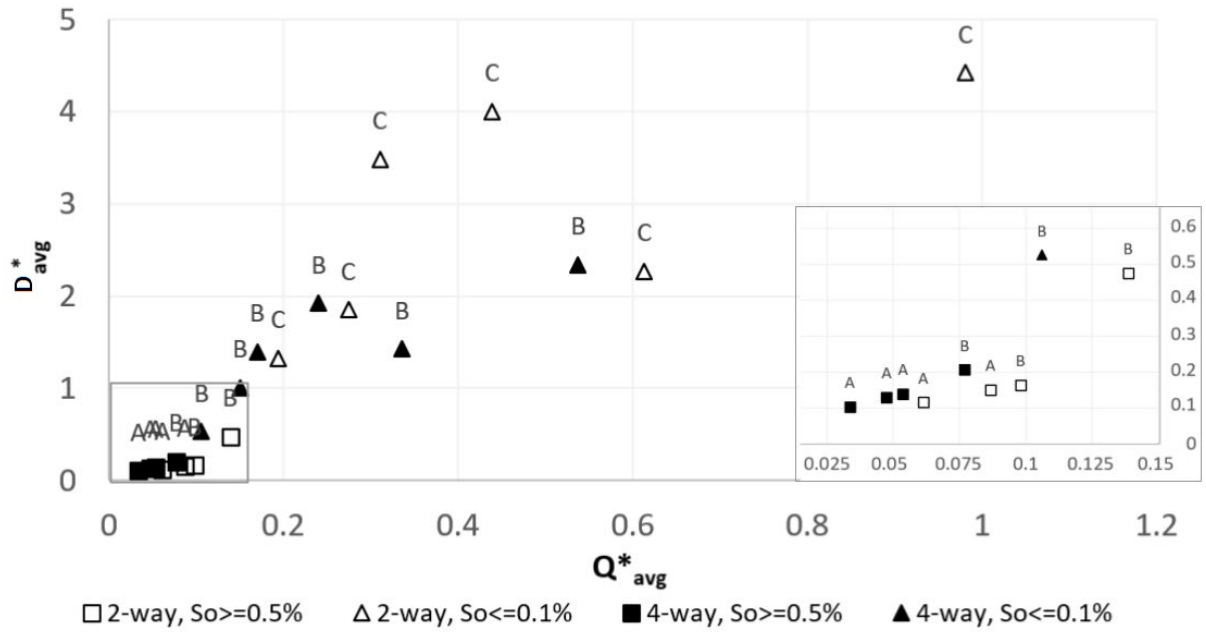


Figure 8: Relationship between D_{avg}^* and Q_{avg}^* for the conditions involving $Q_{inflow} = 2.1 \text{ m}^3/\text{s}$. The figure inset presents the details for the cases with lower Q_{avg}^* values, with the letters indicating the pressurization types.

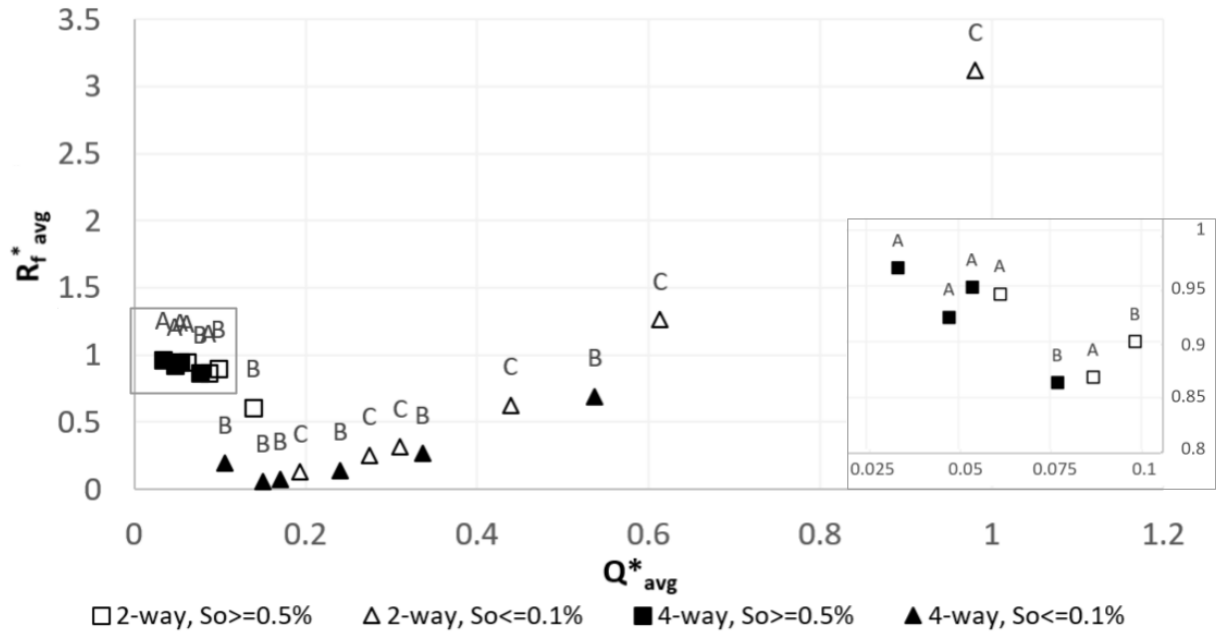


Figure 9: Relationship between the $R_{f,avg}^*$ and Q_{avg}^* for the cases using $Q_{inflow} = 2.1 \text{ m}^3/\text{s}$. The inset presents the details for the cases with smaller Q_{avg}^* values.

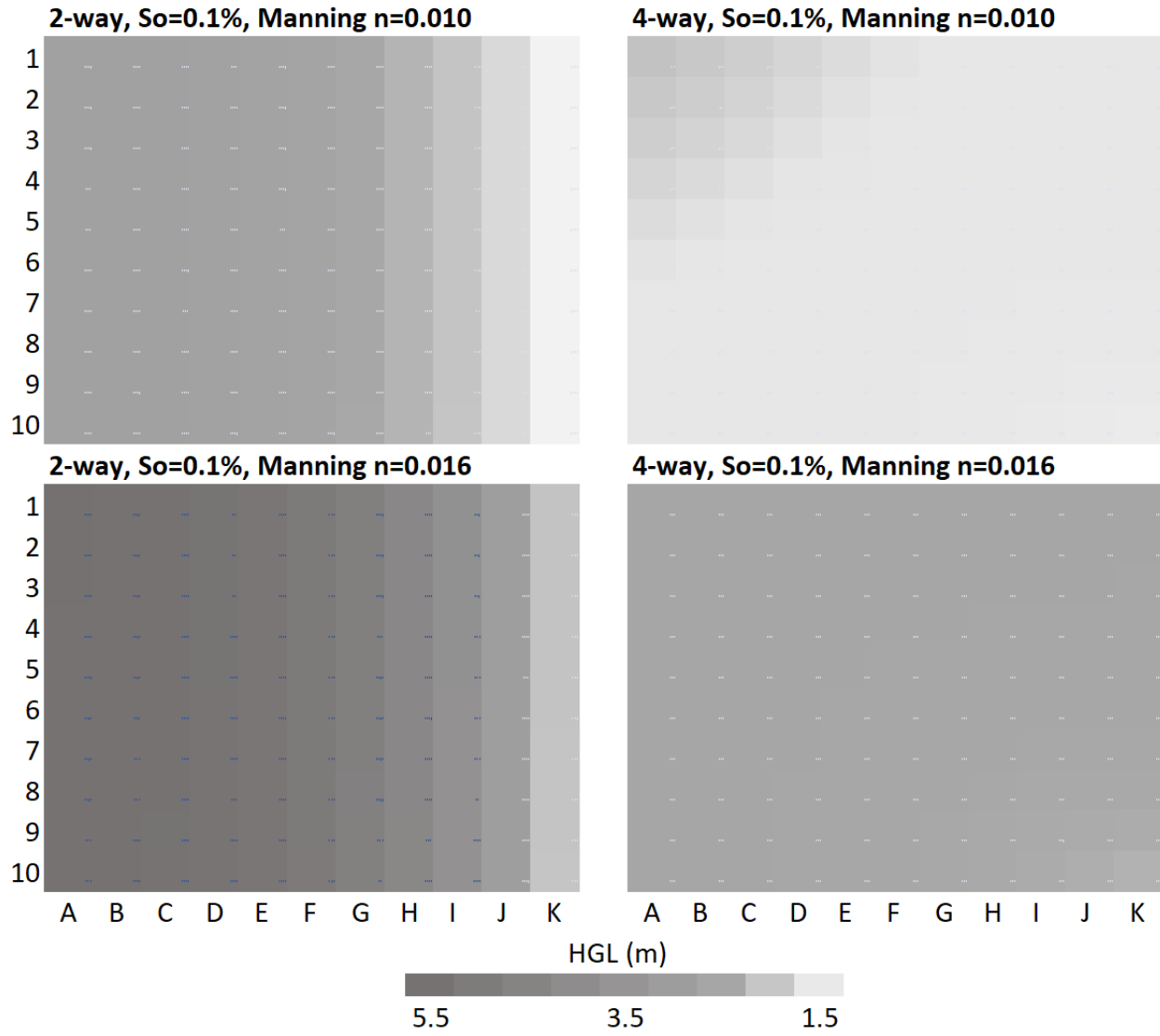


Figure 10: Plan view of HGL values at junctions for four SCNs with $S_o = 0.1\%$ indicating the variation in the head distribution according to the connectivity and Manning roughness.

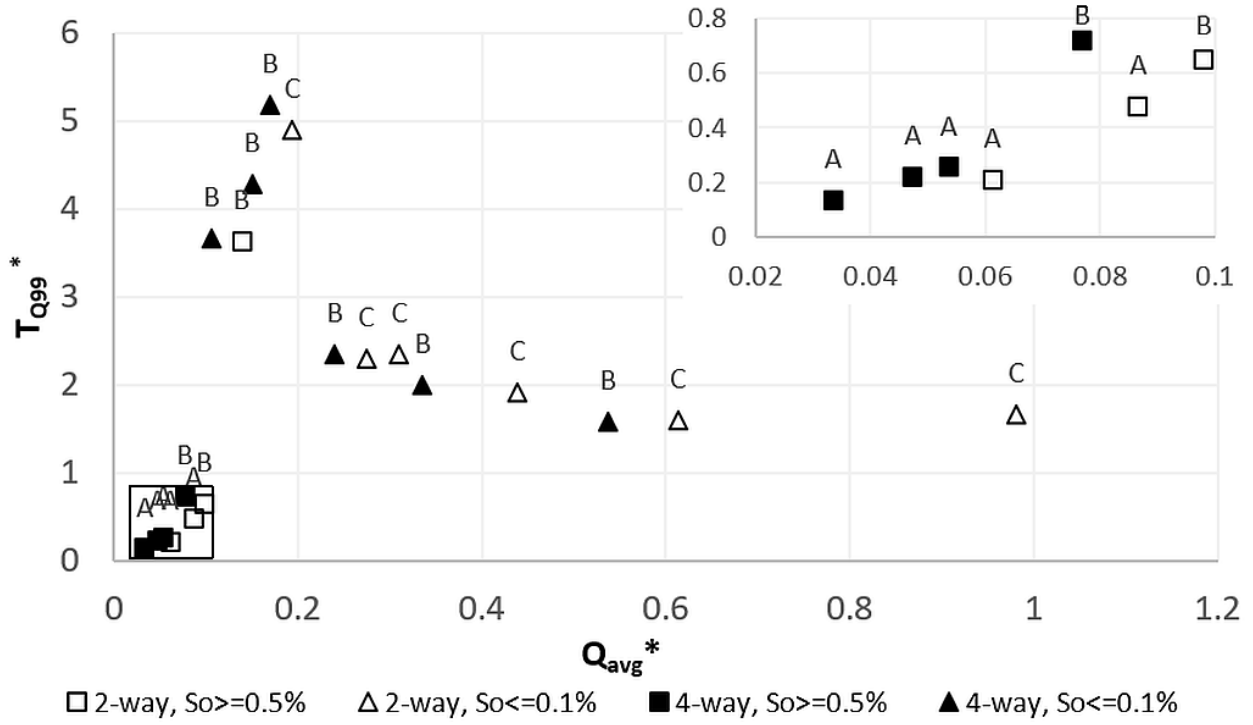


Figure 11: Relationship between the T_{Q99}^* and Q_{avg}^* for the conditions involving $Q_{inflow} = 2.1 \text{ m}^3/\text{s}$. The figure inset presents the details for the cases with lower Q_{avg}^* values.

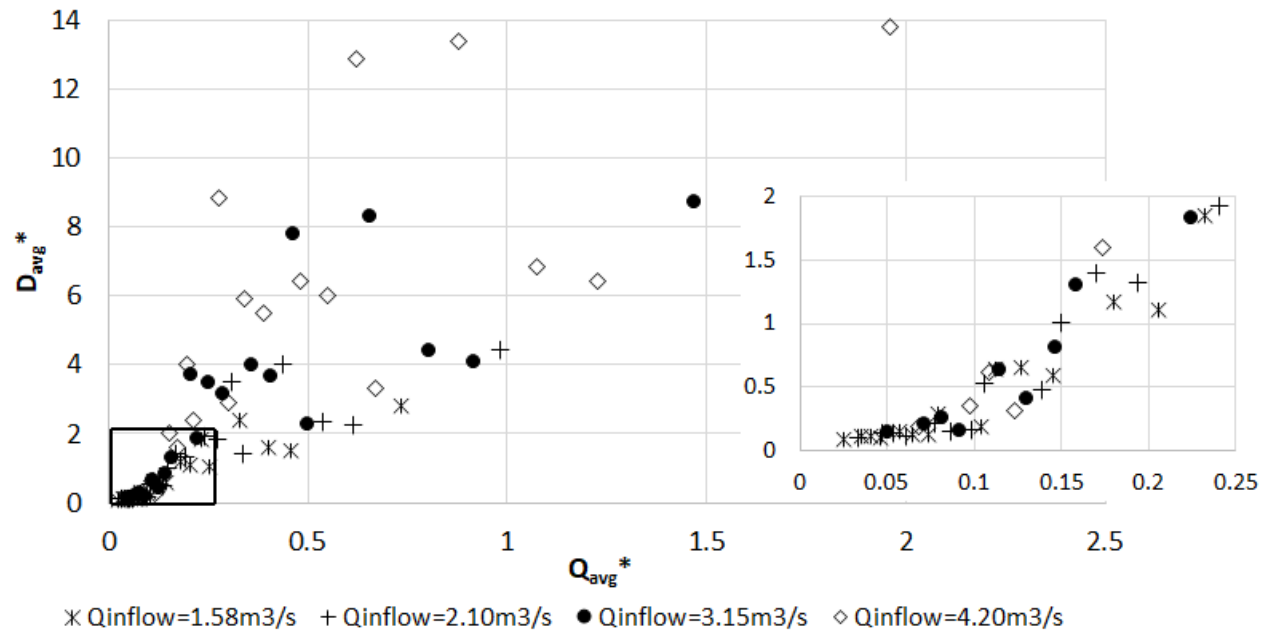


Figure 12: Relationship between D_{avg}^* and Q_{avg}^* for all inflow conditions. The figure inset presents the details for the cases with lower Q_{avg}^* values.

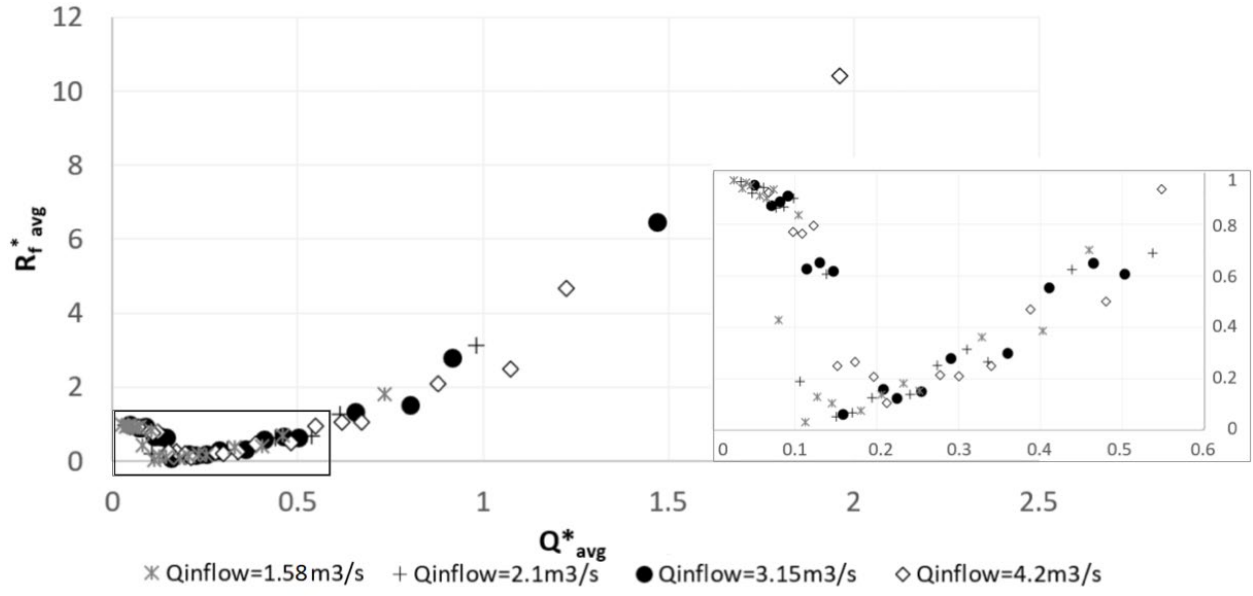


Figure 13: Relationship between the $R_{f,avg}^*$ and Q_{avg}^* for all inflow conditions. The inset presents the details for the cases with smaller Q_{avg}^* values.

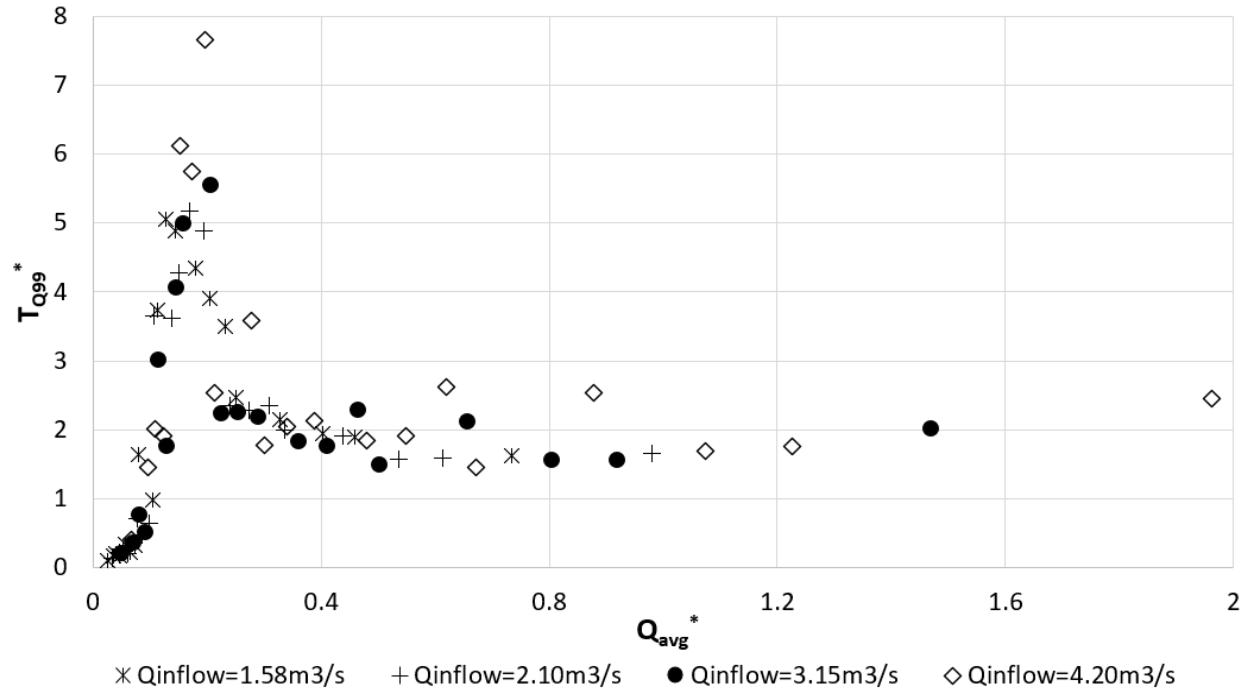


Figure 14: Relationship between the T_{Q99}^* and Q_{avg}^* for all inflow conditions. Note that peak T_{Q99}^* values increased with Q_{inflow} , but all peak values occurred near Q_{avg}^* equal to 0.20.

65

Table 1: Variables used in this investigation with associated tested range.

Variable	Tested range
SCN topology	two-way (2w) and four-way (4w) connectivity, as shown in Figure 1.
Conduit slope S_o	0.01%, 0.05%, 0.10%, 0.50%, 1.0%
Q_{inflow}	Uniform inflow at all junctions with the summation of all junction inflow rates equal to 2.10 m ³ /s (baseline), 1.58 m ³ /s, 3.15 m ³ /s, and 4.20 m ³ /s. These values correspond to rainfall intensities ranging from 4.70 to 12.5 mm/hr.
Manning roughness n	0.010 and 0.016

66

67

68 **Table 2:** Q_{max}^* values and observed pressurization type for all simulated conditions. Results are grouped by SCN
69 topology and Manning roughness.

SCN Topology	Manning roughness	Slope (%)	Q_f (m^3/s)	Q_{max}^* values for all Q_{inflow} values and corresponding SCN pressurization type observed							
				$Q_{inflow}=1.57$ m^3/s		$Q_{inflow}=2.10$ m^3/s		$Q_{inflow}=3.15$ m^3/s		$Q_{inflow}=4.20$ m^3/s	
2w	0.010	0.01	0.31	5.05	C	6.74	C	10.11	C	13.48	C
2w	0.010	0.05	0.70	2.26	C	3.01	C	4.52	C	6.03	C
2w	0.010	0.10	0.99	1.60	B	2.13	C	3.20	C	4.26	C
2w	0.010	0.50	2.20	0.71	A	0.95	A	1.43	B	1.91	B
2w	0.010	1.00	3.12	0.51	A	0.67	A	1.01	A	1.35	B
4w	0.010	0.01	0.31	5.05	B	6.74	B	10.11	B	13.48	B
4w	0.010	0.05	0.70	2.26	A	3.01	B	4.52	B	6.03	B
4w	0.010	0.10	0.99	1.60	A	2.13	B	3.20	B	4.26	B
4w	0.010	0.50	2.20	0.71	A	0.95	A	1.43	B	1.91	B
4w	0.010	1.00	3.12	0.51	A	0.67	A	1.01	A	1.35	B
2w	0.016	0.01	0.19	8.09	C	10.78	C	16.17	C	21.56	C
2w	0.016	0.05	0.44	3.62	C	4.82	C	7.23	C	9.64	C
2w	0.016	0.10	0.62	2.56	C	3.41	C	5.11	C	6.82	C
2w	0.016	0.50	1.38	1.14	A	1.52	B	2.29	B	3.05	B
2w	0.016	1.00	1.95	0.81	A	1.08	B	1.62	B	2.16	B
4w	0.016	0.01	0.19	8.09	B	10.78	B	16.17	B	21.56	B
4w	0.016	0.05	0.44	3.62	B	4.82	B	7.23	B	9.64	B
4w	0.016	0.10	0.62	2.56	B	3.41	B	5.11	B	6.82	B
4w	0.016	0.50	1.38	1.14	A	1.52	B	2.29	B	3.05	B
4w	0.016	1.00	1.95	0.81	A	1.08	A	1.62	B	2.16	B

70